








Direct imaging of distorted vortex structures and magnetic vortex annihilation processes in ferromagnetic/antiferromagnetic disk structures

Sri Sai Phani Kanth Arekapudi ^{1,*}, Benny Böhm,¹ Lakshmi Ramasubramanian ^{1,2}, Fabian Ganss,¹ Peter Heinig,¹ Sven Stienen,² Ciarán Fowley ², Kilian Lenz ², Alina M. Deac,² Manfred Albrecht ³, and Olav Hellwig ^{1,2}

¹*Institute of Physics, Technische Universität Chemnitz, 09107 Chemnitz, Germany*

²*Institute of Ion Beam Physics and Materials Research, Helmholtz-Zentrum Dresden-Rossendorf, Bautzner Landstrasse 400, 01328 Dresden, Germany*

³*Institute of Physics, University of Augsburg, Universitätsstraße 1, 86159 Augsburg, Germany*

 (Received 7 July 2020; revised 8 December 2020; accepted 10 December 2020; published 6 January 2021)

Chiral spin textures, such as skyrmions, merons, and vortices in ferromagnetic (FM)/antiferromagnetic (AFM) heterostructures are actively explored for utilization in future data storage and signal processing devices. Here, we present a systematic study of the magnetic vortex structures in soft-magnetic NiFe and exchange coupled NiFe/IrMn and IrMn/NiFe/IrMn disk structures. The annihilation of the magnetic vortex state is mediated by the creation and subsequent annihilation of the intermediate vortex-antivortex (V-AV) pairs. Using the combination of high-resolution in-field magnetic force microscopy (MFM) and magneto-optic Kerr effect magnetometry, we show a considerable enhancement in the stability of the intermediate V-AV state in exchange coupled NiFe/IrMn and IrMn/NiFe/IrMn disk structures. Analysis of the remanent high-resolution MFM images shows a significant increase in the effective vortex core radius and an additional distortion of the FM vortex structure in exchange coupled disks, most likely caused by the randomly distributed uncompensated spins at the surface of the AFM layer. We further suggest that the displacement of the vortex core from the center of the exchange coupled disks depend on the magnitude of the exchange bias field and AFM grain characteristics. Additionally, we present a summary of crucial magnetic vortex parameters and properties, such as effective core radius, core displacement, handedness, nucleation field, V-AV annihilation field, and interfacial exchange energy in exchange coupled disk structures.

DOI: [10.1103/PhysRevB.103.014405](https://doi.org/10.1103/PhysRevB.103.014405)

I. INTRODUCTION

The interfacial exchange interaction between an anti-ferromagnet and a ferromagnet leading to the so-called exchange bias (EB) effect [1] has triggered tremendous interest for its fundamental physics as well as for its impact on applications [2]. In the exchange coupled ferromagnetic (FM)/antiferromagnetic (AFM) heterostructures, the FM layer is pinned by the randomly distributed uncompensated spins at the surface of the AFM thin film [3,4]. This results in a shift of the FM hysteresis loop in the magnetic field axis referred to as the EB field. Heterostructured FM/AFM systems are used in modern spintronics circuits [5], skyrmion-based spin-torque nano-oscillators [6], low current density magnetic tunnel junctions (MJTs) [7], magnetic vortex-based sensors [8], and neuromorphic devices [9]. Furthermore, AFM thin films can stabilize skyrmions [10] and other chiral spin textures in FMs at zero magnetic field [11–13], which are proposed as an efficient alternative to the current data storage, transport, and signal processing technologies [13–16].

Although EB effects in magnetic vortex structures have been extensively investigated [17–25], a detailed experimental study of the vortex-antivortex (V-AV) mediated

magnetic vortex annihilation processes in FM/AFM [11] and AFM/FM/AFM disk structures is still lacking. The topology of the magnetic vortex structure is determined by the in-plane curling of the magnetization around the center, described by the winding number $w = +1$ (for an antivortex $w = -1$) [26–28]. The out-of-plane magnetization direction at the center of the core is described by the polarization $p = \pm 1$ [27–29]. The topological skyrmion charge of a vortex structure can be parametrized as $q = wp/2$ [28,30,31,32]. The rotational direction of the local magnetization vector in the plane, either clockwise (CW) or anticlockwise (ACW) is characterized by the so-called circularity $c = -1$ and $+1$, respectively [31,32]. The handedness of the vortex is defined by the product $cp = \pm 1$ [31–34]. In a magnetic vortex structure with a lack of symmetry breaking magnetic energy contribution known as Dzyaloshinskii-Moriya interaction (DMI), four degenerate ground states can occur with two possible orientations of p and c [32–36].

The magnetic vortex reversal process is mediated by the spontaneous creation and annihilation of V-AV pairs [27,37–39]. Hertel and Schneider [27] proposed two distinct V-AV pair annihilation mechanisms depending on the relative polarization of the V and AV cores [28,38]. In the first case, with the parallel polarization of the V and AV cores [37], the total topological skyrmion charge of the V-AV pair becomes zero ($q = 0$) [28]. Such a topologically trivial V-AV pair can

*phani.arekapudi@physik.tu-chemnitz.de

be continuously deformed into a uniform magnetization state [37]. In the second case, with antiparallel core polarization of the V and AV pair, the total skyrmion number of the V-AV pair becomes either +1 or -1 [27,28]. A topologically nontrivial V-AV pair cannot be continuously deformed into a uniform state without involving a magnetic point defect (singularity) referred to as a Bloch point (BP) [27,30,37–42]. Due to the completely vanishing local magnetization [30,42], direct imaging of a BP magnetic structure is considered challenging [43]. However, imaging the nontrivial magnetic-spin textures, such as vortex-domain walls [43] and skyrmion coalescence/separation that supports BPs [44], combined with the micromagnetic simulations is a generally accepted approach.

In this study, we performed real-space imaging of the *distorted vortex structures* proposed by Gilbert *et al.* [17] in exchange coupled FM/AFM disk structures. We study the impact of interfacial exchange coupling between a FM (NiFe) and an AFM (IrMn) on the V-AV mediated magnetic vortex annihilation process. We further quantify the critical differences between the vortex ground state and V-AV state in FM, FM/AFM, and AFM/FM/AFM disk structures. We employ a combination of in-field high-resolution magnetic force microscopy (HR-MFM) and magneto-optical Kerr effect (MOKE) magnetometry with a microfocused beam, as well as micromagnetic simulations to study the magnetic vortex reversal process. We prepared an array of magnetostatically noninteracting magnetic disk structures with a diameter of 4 μm each and a center-to-center distance (pitch) of 12 μm . The disk structures are made out of soft-magnetic $\text{Ni}_{81}\text{Fe}_{19}$ (from now on referred to as NiFe) with a thickness of 40 nm, known to yield a low (micromagnetic) energy vortex ground state [29,32,33,45–47]. As an AFM, we use $\text{Ir}_{30}\text{Mn}_{70}$ (referred to as IrMn) 7.5 nm thick.

II. EXPERIMENT

The disk structures were fabricated on a high resistive commercial *p*-type Si(100) substrate with a 4-nm-thick native SiO_2 layer, using the lift-off process. The thin film multilayers were deposited using DC magnetron sputtering with Ar as sputter gas ($p_{\text{Ar}} = 3 \mu\text{bar}$). For all the samples in the study, a Ta (5 nm) seed layer was used to improve the adhesion of the functional materials with the substrate and to promote (111) texture in the NiFe thin films. The functional FM and AFM layers were deposited from 4N purity $\text{Ni}_{81}\text{Fe}_{19}$ and $\text{Ir}_{23}\text{Mn}_{77}$ alloy targets at a deposition rate of 0.3 $\text{\AA}/\text{sec}$. The deposition rates were precalibrated by x-ray reflectivity (XRR) measurements and controlled via a quartz microbalance (monitor) during the deposition. Rutherford backscattering spectroscopy (RBS) on sputter-deposited reference thin films revealed the atomic stoichiometry of $\text{Ni}_{100-x}\text{Fe}_x$ with $x = 19(\pm 1)$ at. % and $\text{Ir}_x\text{Mn}_{100-x}$ with $x = 30(\pm 1)$ at. %.

In the case of a simple FM disk structure, a Pt (2 nm)/Ta (8 nm) bilayer was used as a cap layer. In the remaining samples with the AFM (IrMn) layer, we use Ta (2.5 nm) as a cap layer to protect the functional layers from oxidation. All the samples were designed so that the FM layer is consistently 10 nm below the top surface, which is crucial for a direct comparison of the magnetic contrast obtained from the

MFM scans for different samples in the study. Bragg scans performed using x-ray diffraction revealed a chemically disordered face-centered-cubic (fcc) structure with a strong (111) texture for both NiFe ($2\theta = 44.22^\circ$) and IrMn ($2\theta = 41.12^\circ$) layers [see Supplemental Material Figs. S1(a)–S1(c) [48]]. Additionally, we obtain a rocking width of $\Delta\Omega \approx 3.63^\circ$ for the NiFe layer and $\Delta\Omega \approx 4.35^\circ$ for the IrMn layer along the (111) orientation [see Supplemental Material Fig. S1(d) [48]].

The field cooling (FC) and zero-field cooling (ZFC) experiments were performed using a superconducting quantum interference device vibrating sample magnetometer (SQUID-VSM) with a temperature range of 1.5–1000 K and a maximum magnetic field up to ± 7 T. In the FC state, the samples were heated from 300 to 605 K in a magnetic field of +7 T applied in the film plane, and the samples were kept at 605 K for 90 min (field annealing). Later, the samples were field cooled down to 300 K in +7 T magnetic field. In the ZFC state, after heating the sample to 605 K, the samples underwent an alternating magnetic field cycling, a so-called AC demagnetization routine. Starting from +7 T, we reduce the magnetic field in 3% steps to the negative magnetic field direction and vice versa (closely following an exponentially decaying triangular function) until the magnetic field reaches close to zero. At zero magnetic field, the samples were annealed for 90 min, followed by the zero-field cooling to 300 K. For consistency, the samples without the AFM layer underwent a similar ZFC demagnetization procedure. The heating and cooling rates were kept constant at 15 K/min for both FC and ZFC procedures. After the FC/ZFC procedure, samples were field cycled between +7 T and -7 T and vice versa ten times to overcome the training effect [49,50], prior to the MOKE and MFM measurements.

A commercial nano-MOKE 2 setup equipped with a He-flow cryostat with a temperature range of 4.5–510 K was used in the study. All the magnetic hysteresis loops shown in the study were obtained in longitudinal geometry with a magnetic field range of ± 0.5 T in the film plane. A red laser with a wavelength of 635 nm and a spot size of $< 10 \mu\text{m}$ was used to obtain the MOKE hysteresis loops.

In-field high-resolution magnetic force microscopy (HR-MFM) imaging was performed using a NanoScan MFM. A commercial (Team Nanotec) high-resolution Si tip uniformly coated with a low magnetic moment CoCr alloy operating at a high resonance frequency $f_0 = \omega_0/2\pi = 128.515$ kHz at an oscillation amplitude of 2.5 nm and spring constant $C = 0.7$ N/m was used in the MFM imaging experiments. The measurements were performed in an HV chamber to increase the sensitivity and Q factor of the tip (> 20000). The MFM scans were performed in noncontact (NC) mode while maintaining a constant height of $\sim 10(\pm 2)$ nm between the dynamically oscillating magnetic tip and the sample surface. The electrostatic potential and the thermal drift between the metallic tip and the sample surface were actively compensated. Within the interaction volume V , the three-dimensional (x, y, z) force component acting on the dynamically oscillating magnetic tip due to the magnetic interactions with the stray field of the sample in reciprocal space is given by $F_z(n) = -\mu_0 \int M_{\text{FM-tip}}(x', y', z') d/dz' H_{\text{sample}}[(x', y', z') + r] dV'$ [51], where $M_{\text{FM-tip}}$ is the tip magnetization, $\mu_0 H_{\text{sample}}$ is the stray field at the sample surface, and

$n = (n_x, n_y, n_z)$ is the location of the tip. The highest sensitivity of the magnetic tip is to the z' component, which is at the apex of the tip, giving rise to the out-of-plane (OOP) component of the MFM scan. Away from the apex, which accounts for the x' and y' in-plane (IP) components, the sensitivity of the tip drops dramatically. The relative shift in the resonant frequency of the tip due to the force derivative is given by $\Delta\omega = \omega_0 1/2C(\partial F_z/\partial z)$ [51,52]. An attractive magnetic force gives rise to a negative shift, and a repulsive force gives rise to a positive shift in ω_0 . The magnetic field experienced by the magnetic vortex structure during the in-field MFM scan is the vector sum of the static external magnetic field $\mu_0 H_{\text{app}}$ and the effective stray field of the tip $\mu_0 H_{\text{tip}}$ given by $\mu_0 H_T = \mu_0 H_{\text{app}} + \mu_0 H_{\text{tip}}$. To achieve magnetic vortex annihilation in the hard-axis (OOP) direction, one would need a rather large OOP fields up to $\mu_0 H_K = 1.2$ T, i.e., the contribution from the nonzero OOP field component originating from the $\mu_0 H_{\text{app}}$ and $\mu_0 H_{\text{tip}} = 12(\pm 3)$ mT are neglected (unless stated otherwise).

We carried out a series of micromagnetic simulations using the open-source MUMAX3 package [53]. To study the magnetic vortex reversal mediated by the V-AV pair, we consider a disk with 2 μm diameter (to conserve computation time) and 40 nm height, $M_S = 800$ kA/m, exchange stiffness constant $A_{\text{ex}} = 1.3 \times 10^{-12}$ J/m, and uniaxial anisotropy constant $K = 0$. To further study the role of various material properties on the static magnetic field stability of the V-AV state, we have performed additional simulations considering, $A_{\text{ex}} = 1.3 \times 10^{-11}$ J/m and 1.0×10^{-11} J/m, and $K = 0, 0.2 \times 10^3$ J/m³ and 0.4×10^3 J/m³. We choose $1 \times 1 \times 40$ nm³ and $2 \times 2 \times 40$ nm³ cell sizes for disks with 1 and 2 μm diameter, respectively. In Supplemental Material Tables I and II [48], we present a summary of material parameters as well as the obtained exchange energy for the vortex state and the V-AV state.

III. RESULTS AND DISCUSSION

The magnetic vortex annihilation mediated by the creation and annihilation of the V-AV pairs obtained from the micromagnetic simulation is shown in Figs. 1(a)–1(f). Upon applying a static magnetic field along the positive x direction, the initial motion of the core is determined by the vortex handedness (cp) [31]. For $cp = +1$, the core moves orthogonally towards the positive y direction, as shown in Figs. 1(b) and 1(c). The vortex handedness $cp = -1$ results in the motion of the core towards the negative y direction (not shown). Due to the competition between the magnetostatic energy and the Zeeman energy, the core is deflected from the center of the disk to increase the area with magnetic moments aligned parallel to the applied magnetic field direction [46]. The vortex state remains intact, as shown in Fig. 1(c). For small core displacement from the center of the disk, the exchange energy remains almost unchanged [see Supplemental Material Fig. S2 b(ii) [48]]. At a critical applied magnetic field, the V-AV pairs are created to assist the annihilation of the magnetic vortex [37,39] at the expense of additional exchange energy. The formation of the V-AV pairs causes a buckling of the spin texture, as shown in Fig. 1(d). Increasing the magnetic field further results in the annihilation of the V-AV pairs

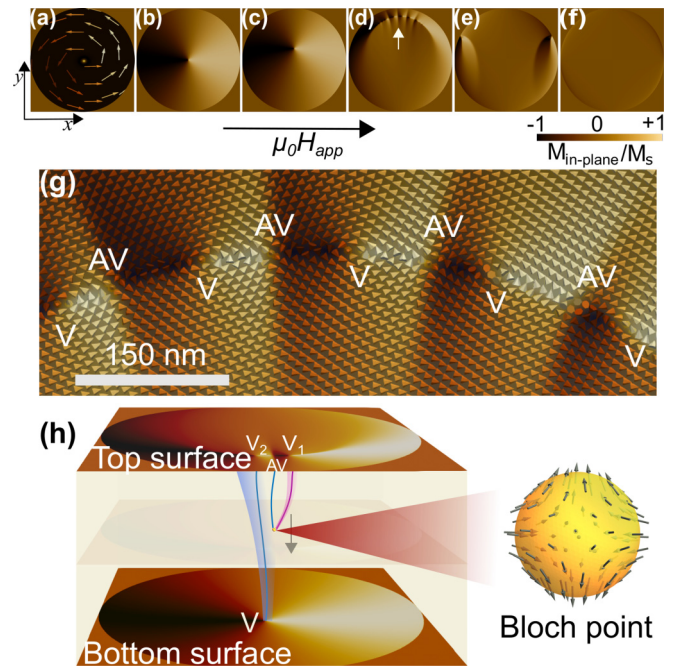


FIG. 1. The magnetic vortex annihilation mediated by the creation and annihilation of the V-AV pairs in a static magnetic field, obtained from the micromagnetic simulation for a disk of 2- μm diameter with handedness $cp = +1$. (a) In-plane (IP) spin structure of the vortex with an out-of-plane (OOP) core polarization $p = +1$. (b), (c) Vortex core deflection in the positive y direction as a consequence of the applied magnetic field in the positive x direction. (d) Subsequent creation of the V-AV pairs, followed by an edge vortex state (e) and saturation state (f). (g) Detailed spin structure of the V-AV pairs overlaid on the buckled IP spin texture from the region indicated by an arrow in (d). (h) Schematic for the injection and propagation mechanism of a BP through the film thickness [57]. The original vortex V_1 ($p = +1$), and the newly nucleated vortex V_2 with opposite core polarization ($p = -1$) [27,28,37,39,57]. An antivortex with polarization $p = -1$ is created to separate the two vortex cores. A spiraling BP structure for $q = +1$ is shown on the right [30,42].

accompanied by the spontaneous decay of exchange energy [27]. Once the V-AV pairs are annihilated, an edge (vortex) state is formed, followed by the saturation of the disk, as shown in Figs. 1(e) and 1(f), respectively. The edge state is characterized by two vortices at the left and the right edge of the disk with opposite core polarization. For a detailed view of the IP and OOP magnetization components of the vortex state, V-AV state, and edge state, as well as the micromagnetic energy terms as a function of the applied magnetic field, see Supplemental Material Figs. S2–S4 [48].

Figure 1(g) shows the spin structure of the V-AV pairs overlaid on the buckled IP magnetic contrast. To understand the elusive creation and annihilation mechanism of the V-AV pairs, we consider a simple V-AV-V triplet consisting of the initial vortex V_1 with polarization $p = +1$ and a newly nucleated vortex V_2 with opposite polarization $p = -1$, separated by an antivortex core with $p = -1$, as shown in Fig. 1(h). Due to the antiparallel polarization of the vortex (V_1) and AV cores [37,39], the total topological skyrmion charge $q_{\text{V-AV}}$ of the V_1 -AV pair adds to a total of $+1$ [28]. The creation

of such a topologically nontrivial V-AV pair requires the spontaneous injection of magnetic point defects, such as BPs [27,28,30,37–42] at the top or the bottom surface of the FM film at the expense of additional exchange energy [27,53]. A BP can be described as a three-dimensional topological invariant singularity of the magnetization field vector, where the local magnetization completely vanishes (IP magnetization $m_x = m_y = 0$ and OOP magnetization $m_z = 0$) [30,40–42]. The structure of a spiraling BP shown in Fig. 1(h) can be obtained from the hedgehog solution [30,42], where the magnetic moments around the unit sphere are rotated by an angle $>90^\circ$ to reduce the magnetostatic energy (see Supplemental Material Fig. S5 [48]). The spiraling BP configuration accommodates the V-AV pair with opposite core polarization [42]. Once the BPs propagate through the film thickness in the OOP direction, the V-AV pairs are annihilated, and an edge vortex state is formed. If we were to assume a parallel polarization of the V_1 -AV cores [37], the total topological skyrmion charge (q_{V-AV}) becomes zero [28]. Such a V-AV spin texture can be continuously deformed into a uniform state without invoking the BPs [28,31,37].

The characteristic length scale l_{BP} of a BP similar to the one shown in Fig. 1(h) is predicted to be far below the exchange length l_{ex} of a given magnetic material [30]. The exchange length [54] of the NiFe (40 nm) reference thin film $l_{ex} = \sqrt{2A_{ex}/\mu_0 M_s^2} = 5.8$ nm, where $A_{ex} = 1.28 \times 10^{-11}$ J/m is the exchange stiffness constant determined from the perpendicular standing spin wave (PSSW) modes using ferromagnetic resonance (FMR) spectroscopy [55]. The saturation magnetization $M_s = 778$ kA/m, as determined by SQUID-VSM.

We now reproduce the magnetic vortex annihilation process mediated by the V-AV pairs experimentally in the disk structures shown in Figs. 2(a)–2(c) for FM: NiFe (40 nm), FM/AFM: NiFe (40 nm)/IrMn (7.5 nm), and AFM/FM/AFM: IrMn (7.5 nm)/NiFe (40 nm)/IrMn (7.5 nm) multilayers, respectively. Figure 2(d) shows the MOKE hysteresis loop for the simple FM disk structures. The inset shows the full hysteresis loop, which is characteristic of the presence of a magnetic vortex state [46,47]. From the descending branch of the MOKE hysteresis loop, we obtain the nucleation field of the FM vortex core $\mu_0 H_n = 14(\pm 1)$ mT, accompanied by an abrupt reduction in the magnetization. The in-field MFM measurements were performed in the ascending branch of the hysteresis loop, as indicated by the black arrowheads in Fig. 2(d). Figure 2(g)(i) shows the remanent magnetic vortex structure. The in-field MFM images corresponding to the V-AV mediated magnetic vortex annihilation process are shown in Figs. 2(g)(ii)–2(g)(vi). Due to the product $cp = (+1)(+1) = +1$, the vortex core continuously deflects in the positive y direction in the film plane orthogonal to the applied magnetic field in the positive x direction, as shown in Figs. 2(g)(ii) and 2(g)(iii). As mentioned earlier, to assist the magnetic vortex annihilation process, the V-AV pairs are formed at a critical magnetic field of about $16(\pm 1)$ mT. Figure 2(g)(iv) shows the MFM image corresponding to the *buckled (V-AV) state*. In the next step, we increase the applied magnetic field $\mu_0 H_{app}$ only by about 2 mT. As a result, the V-AV pairs are annihilated, forming an *edge state* shown in Fig. 2(g)(v). When the applied magnetic field reaches the saturation field,

the FM disk stabilizes in a single-domain (saturated) state [see Fig. 2(g)(vi)].

We repeated the in-field MFM measurements to determine the static magnetic field stability of the V-AV state in the FM disk. The buckled (V-AV) spin structure reappeared at $\mu_0 H_{app} \approx +15(\pm 1)$ mT [see Fig. 2(g)(iv)]. By repeating the MFM scan (keeping $\mu_0 H_{app}$ constant at +15 mT), the V-AV state degenerated into an edge state, which indicates a somewhat unstable (volatile) nature of the V-AV state. The stray field of the magnetic tip ($\mu_0 H_{tip}$) that the disk is exposed to during the scan is sufficient to annihilate the V-AV pairs [56].

To further understand the V-AV mediated magnetic vortex annihilation process and the stability of the V-AV pairs in a static magnetic field, we performed a series of micromagnetic simulations. We considered the exchange stiffness constant similar to the experimental values $A_{ex} = 1.3 \times 10^{-11}$ J/m and 1.0×10^{-11} J/m. The V-AV state is not stable in the static magnetic field regime. The vortex state spontaneously decays into an edge state, as shown in Supplemental Material Fig. S2(a) [48]. Once the BPs are injected at the surface of the FM disk to assist the creation of the topologically nontrivial V-AV pairs, they tend to spontaneously propagate through the film thickness in the OOP direction, resulting in the annihilation of the V-AV pairs [27,30,39,57]. Increasing the uniaxial anisotropy of the NiFe thin film [23] in the micromagnetic simulations (e.g., $K = 0, 0.2 \times 10^3$ J/m³ and 0.4×10^3 J/m³) did not stabilize the V-AV pairs. In contrast, we were able to image the V-AV state in the NiFe disks as shown in Fig. 2(g)(iv). Kim and Tchernyshyov [30] proposed a theoretical mechanism of pinning the BPs by the inevitable lattice defects/imperfections in the FM thin films. As BPs are scale-invariant ($l_{BP} \ll l_{ex}$) it is conceivable that the spatially varying magnetization of the propagating BP can be pinned by the fcc lattice defects/imperfections along the thickness of the film (in the OOP direction) [30]. Such a mechanism of pinning the BPs and the dipolar interactions can stabilize the intermediate V-AV pairs from degeneracy for a limited magnetic field range.

Alternatively, we consider $A_{ex} = 1.3 \times 10^{-12}$ J/m in the micromagnetic simulations. As a result, we observe a significant increase in the magnetic field stability of the V-AV pairs, most likely due to the dipolar interactions. The exchange energy for the vortex state, V-AV state, and various geometric and material parameters considered in the micromagnetic simulations are listed in Supplemental Material Tables I and II [48]. Experimentally, tuning A_{ex} of NiFe thin films is beyond the scope of this work. For example, Salikhov *et al.* [58] showed that it is possible to tune A_{ex} of $(\text{Ni}_{81}\text{Fe}_{19})_{100-x}\text{Gd}_x$ alloy thin films by systematically varying x .

Increasing the static magnetic field stability of the V-AV pairs (or 1D domain walls) is highly desirable from an application point of view. For instance, nontrivial spin textures, such as V-AV domain walls, can overcome the Walker-breakdown limit [59], which is crucial for significantly increasing the operating frequency range of domain wall based spintronic and magnonic devices [59–61]. Due to the intrinsic and transient nature of the BP mediated V-AV state [27,39,57], thus far it was not possible to extend the magnetic field range of the BP mediated V-AV state without significantly changing the geometry of the magnetic micro or

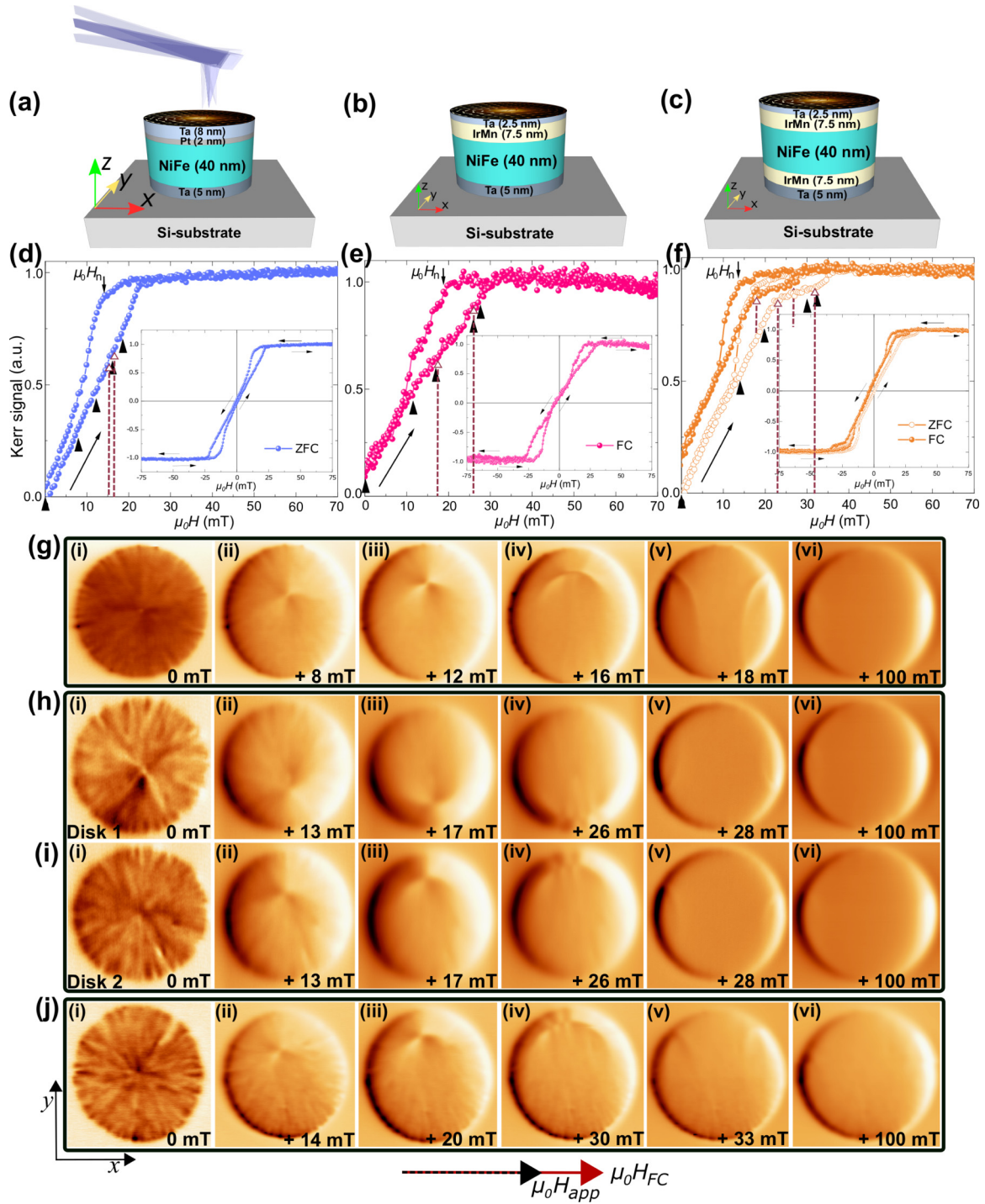


FIG. 2. Disk structures and the corresponding hysteresis loops, and in-field HR-MFM image sequences. (a)–(c) Disk structures with 4 μm diameter investigated in this study consisting of a simple FM, AFM/FM, and AFM/FM/AFM, respectively. Scanning electron microscopy (SEM) images of the patterned disk arrays are shown in Supplemental Material Fig. S6 [48]. (d)–(f) Longitudinal MOKE hysteresis loops obtained at 300 K for the FM, AFM/FM, and AFM/FM/AFM disk structures after FC and ZFC procedure, as indicated. The full hysteresis loops are shown as an inset. The brown dashed lines indicate the magnetic field region where the V-AV state can be stabilized. Black arrowheads indicate the magnetic field values at which the in-field MFM images were obtained. In-field MFM image sequences for the simple FM case (g)(i)–(g)(vi), the FM/AFM case for disk 1 (h)(i)–(h)(vi), and disk 2 (i)(i)–(i)(vi), and the AFM/FM/AFM case (j)(i)–(j)(vi) are shown.

nanostructures [62,63]. For example, in soft-magnetic elliptical (stadium shaped) nanostructures, V-AV-V triplet structures can be stabilized at zero magnetic field [63]. Alternatively, we show in the current study that it is possible to extend

the static magnetic field stability of the intermediate (or transient) V-AV state using the interfacial exchange coupling between a FM and an AFM layer, even in circular disk-shaped structures.

We now turn the attention to the exchange coupled FM/AFM disk structures shown in Fig. 2(b), where an (AFM) IrMn (7.5 nm) layer is introduced at the top surface of the NiFe (40 nm) disk structure. Figure 2(e) shows the longitudinal MOKE hysteresis loop, for the exchange coupled FM/AFM: NiFe (40 nm)/IrMn (7.5 nm) disk structure after the FC process. We extract the EB field $\mu_0 H_{\text{eb}} = -2.5$ mT from the loop shift of the full MOKE hysteresis loop shown as an inset in Fig. 2(e). Due to the inverse scaling of $\mu_0 H_{\text{eb}}$ with respect to the FM film thickness t_{FM} ($\mu_0 H_{\text{eb}} \propto 1/t_{\text{FM}}$) [1,64], we expect a small loop shift. From the descending branch of the MOKE hysteresis loop, we obtain the nucleation field [17] of the exchange biased vortex $\mu_0 H_n = 18(\pm 1)$ mT. We obtain the in-field MFM images closely following the ascending branch of the magnetic vortex hysteresis loop, as indicated by the black arrowheads in Fig. 2(e). The remanent and in-field MFM images for the exchange coupled disk 1 ($cp = -1$) and disk 2 ($cp = +1$) are shown in Figs. 2(h) and 2(i), respectively.

At remanence for disk 1, we observe that the core is deflected in the negative y direction by about 270 nm from the center of the disk (orthogonal with respect to the cooling field $\mu_0 H_{\text{FC}}$ direction), as shown in Fig. 2(h)(i). However, in disk 2 shown in Fig. 2(i)(i), for the same $\mu_0 H_{\text{FC}}$ direction, the vortex core is deflected in the positive y direction by about 210 nm from the center of the disk. At remanence, the displacement of the vortex core position from the center of the exchange coupled FM/AFM disks Δd_{core} (so-called *tilted vortex*) [17,21,22] depends on the magnitude of the exchange bias field [17,18,21–23], and the local AFM grain properties [17,65]. In contrast, the direction of the vortex core deflection in either the positive or negative y direction is determined by the handedness of the vortex structure [23,24]. The handedness (or chirality) protection in exchange coupled FM/AFM disks and thin films were addressed in earlier studies [23,24,66]. In the exchange coupled FM/AFM disks, the competition between the radial spin alignment of the FM vortex structure and the sporadically canted (non-planar) spin structure of the polycrystalline AFM [67,68], in addition to the orange peel coupling [69,70], results in a radial starlike pattern with spatially alternating contrast, which we call a *distorted vortex structure* [17]. Moreover, the evolution of the FM vortex structure is correlated to the randomly distributed uncompensated spins at the surface of the AFM layer [71,72]. Additionally, remanent MFM experiments on FM/AFM disk structures as a function of AFM film thickness t_{AFM} , revealed that the distorted vortex structure is present in FM/AFM disks with $t_{\text{AFM}} > 4.0$ nm, which is generally associated with the AFM film thickness dependent onset of the EB field [17,21,22,64,73]. A tilted vortex structure [21,22] is only observed in exchange coupled disks with $t_{\text{AFM}} \geq 5.5(\pm 0.5)$ nm.

The V-AV mediated magnetic vortex annihilation processes for the exchange coupled FM/AFM disks 1 and 2 are shown in Figs. 2(h)(ii)–2(h)(vi) and 2(i)(ii)–2(i)(vi). The V-AV state was stable in disks 1 and 2 between $18(\pm 1)$ and $26(\pm 1)$ mT. In comparison, the V-AV state was volatile [$\mu_0 H_a \approx 15(\pm 1)$ mT] in the FM disks. We observe an increase in the V-AV state stability field range to $\sim 8(\pm 1)$ mT in the exchange coupled FM/AFM disks (see Supplemental

Material Movie 1 [48]). From the ascending branch of the MOKE hysteresis loop and the in-field MFM study, we obtain the V-AV annihilation field $\mu_0 H_a \approx 27(\pm 1)$ mT.

Figure 2(c) shows the AFM/FM/AFM disk structure. The characteristic MOKE hysteresis loops after FC and ZFC procedures are shown in Fig. 2(f). In the FC state, a definite shift in the vortex hysteresis loop by $\mu_0 H_{\text{ex}} = -4.5$ mT is detectable, whereas no loop shift is present after the ZFC procedure. Due to the presence of randomly distributed uncompensated spins at the surface of the top and bottom AFM layers [71,72,74–76], the FM vortex and the V-AV structure are pinned from both sides. Therefore, we see an additional enhancement in the magnetic field stability of the V-AV state [up to $11(\pm 1)$ mT] in both FC and ZFC states. This becomes apparent in the ascending branch of the MOKE hysteresis loop shown in Fig. 2(f), where an intermediate plateau is present (indicated by the brown-colored dashed line). From the descending branch of the MOKE hysteresis loops shown in Fig. 2(f), we obtain $\mu_0 H_n \approx 14(\pm 1)$ mT and $18(\pm 1)$ mT in the FC and ZFC states, respectively. The remanent and in-field MFM image sequence for the AFM/FM/AFM disk structure is shown in Fig. 2(j). The AFM/FM/AFM disks were field cooled in the positive x direction. Due to the vortex handedness $cp = +1$, we see a deflection of the vortex core from the center of the disk in the positive y direction by about 160 nm. Similar to the FM/AFM disks, we observe a distorted vortex structure at remanence in the AFM/FM/AFM disk structure [see Fig. 2(j)(i)]. We reproduce the V-AV mediated magnetic vortex annihilation process shown in Figs. 2(j)(ii)–2(j)(vi), where we obtain the V-AV annihilation field $\mu_0 H_a \approx 27(\pm 1)$ mT and $31(\pm 1)$ mT in the FC and ZFC states, respectively.

We carried out additional in-field MFM measurements on FM/AFM and AFM/FM/AFM disks to check the stability and reproducibility of the V-AV state. In both cases, the V-AV state remained intact even after repeated in-field MFM scans. To examine the stability of the V-AV state over time, we kept $\mu_0 H_{\text{app}} = +26(\pm 1)$ mT for more than 24 h and performed an additional MFM scan. The V-AV state shown in Figs. 2(h)(iv), 2(i)(iv), and 2(j)(iv) remained intact. The uncompensated spins at the FM/AFM interface [71,72,74–76] are not able to pin the BPs directly, as they tend to propagate along the OOP direction [30,57]. However, uncompensated spins can pin the buckled (V-AV) spin texture at the FM/AFM interface [73–76], whose local pinning potential [77] can be substantial. The applied magnetic field must overcome the interfacial exchange bias field experienced by the V-AV spin structure originating from the FM/AFM interface [71,72,74–76] and the pinning force in the OOP direction experienced by the BPs due to crystal defects [30]. Therefore, we see an increase in the magnetic field stability of the intermediate V-AV state in exchange coupled FM/AFM and AFM/FM/AFM disk structures.

We now address the critical differences between the remanent vortex state and the V-AV state observed in the samples with and without the AFM layers by analyzing the corresponding line profiles, shown in Fig. 3. We have extracted the effective vortex core radius $r_{\text{eff}} \approx 70$ nm from the half width at half maximum (HWHM) of the line profile shown in Fig. 3(a) for the FM disk [78]. The r_{eff} extracted

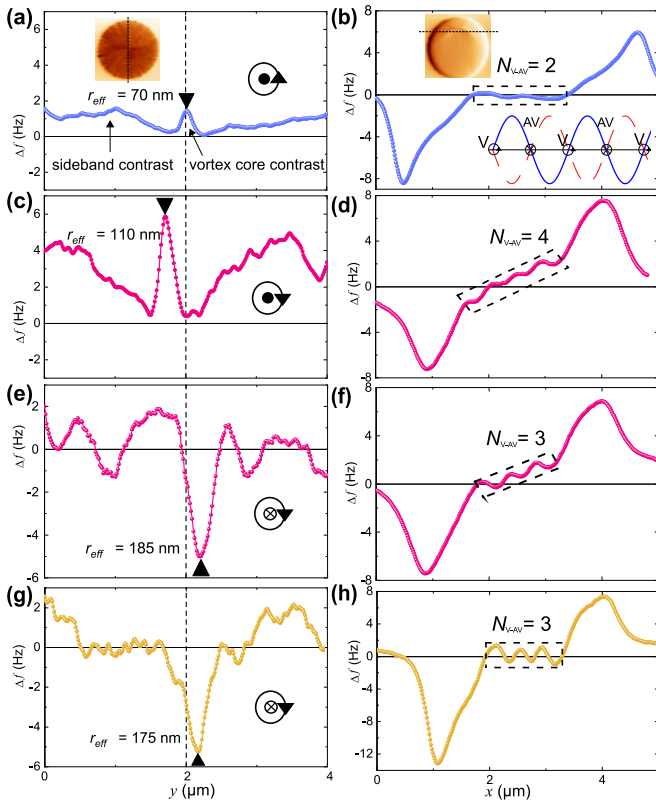


FIG. 3. Line profile extracted from the MFM images for the vortex state at remanence (left column) and the in-field buckled (V-AV) state in FM, FM/AFM and AFM/FM/AFM disks (right column). (a) and (b) Line profile for the vortex core and the buckled (V-AV) spin structure for the FM disk structure. The line profile is extracted from the position shown in the inset MFM images. (c),(d) The line profile for the FM/AFM case, for disk 1 ($cp = -1$), extracted from the MFM images shown in Figs. 2(h)(i) and 2(h)(iv). (e),(f) Similarly, for disk 2 ($cp = +1$), extracted from the MFM images shown in Figs. 2(i)(i) and 2(i)(iv). (g), (h) The line profile for the AFM/FM/AFM disk structures, extracted from Figs. 2(j)(i) and 2(j)(iv). Black triangles indicate the vortex core position on the $4\text{-}\mu\text{m}$ disk. The dashed rectangles indicate the magnetic contrast variation corresponding to the buckled (V-AV) spin texture. The inset in (b) shows a guide to the eye for extracting the number of V-AV pairs from the line profile of the buckled spin texture.

from the line profile of the MFM scans can significantly deviate from the true magnetic vortex core radius r_c , most likely due to the instrument broadening [29,78,79]. Therefore, we provide a numerical estimate of the minimum vortex core radius [80,81] $r_c = (l_{\text{ex}}^2 R / 12\kappa\beta)^{1/3} \approx 14\text{ nm}$, $R = 2\text{ }\mu\text{m}$ is the radius of the disk, $\kappa = 4.12 \times 10^{-2}$ is a numerical constant [80], $L = 40\text{ nm}$ is the height of the disk, and $\beta = 50$ is the aspect ratio (R/L). The numerical estimate $r_c \approx 14\text{ nm} \approx 2.41l_{\text{ex}}$ is in decent agreement with previous experimental values [81]. The significant broadening of $r_{\text{eff}} \approx 5r_c$ observed in the MFM experiments can be explained by considering various extrinsic contributions, such as scan height and the shape of the tip apex [51,78,79]. For instance, decreasing the scan height can reduce the deviation between r_{eff} and r_c to a certain degree [78]. However, the stray fields from the dynamically oscil-

ating magnetic tip can significantly displace and modify the vortex core [56], which puts a lower limit on the scan height.

The MFM scans for the FM, FM/AFM, and AFM/FM/AFM disk structures in the study were performed using the same magnetic tip. The total distance between the dynamically oscillating tip and the FM layer is maintained at $\sim 20\text{ nm}$ in all three cases. Therefore, r_{eff} extracted for various disk structures in the study yields a decent measure of the relative changes. Consistently, we detect an increase in r_{eff} for the exchange coupled disk structures, as shown in Figs. 3(c), 3(e), and 3(g).

In Figs. 3(a), 3(c), 3(e), and 3(g), we observe a significant magnetic contrast (Δf) variation corresponding to the sidebands of the distorted vortex structure. The MFM scans obtained in NC mode are free of topographic interference [51,71,72]. If the observed vortex sideband contrast at remanence shown in Figs. 3(a), 3(c), 3(e), and 3(g) is of topographic origin, these features should also be present in the saturated magnetic disk. Unlike magnetostatic interactions, topographic features resulting from the van der Waals interactions between the magnetic tip and the sample are independent of the applied external magnetic field ($\mu_0 H_{\text{app}}$) [51,71,72]. In the case of the simple FM disk shown in Fig. 3(a), due to the high sensitivity of the instrument, we detect only a weak vortex sideband contrast. This sideband contrast can be attributed to the magnetic inhomogeneities and orange peel coupling [69,70] that shows the tendency of the FM spins at the surface (or surface charges) to follow the surface morphology of the disk. In the exchange coupled disk structures, due to the strong interfacial exchange coupling between the randomly distributed (nonplanar) uncompensated spins of the AFM [71,72,74–76] and the IP component of the FM vortex structure, in addition to the orange peel coupling, we observe a significant enhancement of the vortex sideband contrast [see Figs. 3(c), 3(e), and 3(g) and the corresponding MFM images shown in Figs. 2(h)(i), 2(i)(i), and 2(j)(i)].

The magnetic contrast corresponding to the buckled (V-AV) spin texture is relatively weak in the simple FM case, as shown in Fig. 3(b). However, in exchange coupled FM/AFM and AFM/FM/AFM disks, we observe an enhanced magnetic contrast corresponding to the buckled spin texture [highlighted with black-colored dashed rectangles in Figs. 3(d), 3(f), and 3(h)]. The enhanced magnetic contrast can be attributed to the nonplanar interfacial spin structure of the AFM [67,68], which tilts the FM buckled spin structure more towards the OOP direction via interfacial exchange coupling [71,72].

To understand the increase in r_{eff} and the magnetic contrast corresponding to the buckled spin texture in exchange coupled FM/AFM and AFM/FM/AFM disk structures, we must understand the spin order of the γ -phase IrMn layer. Bragg scans obtained from x-ray diffraction measurements confirm a chemically disordered γ -phase IrMn₃, with a strong (111) texture (see Supplemental Material Fig. S1 [48]). For the chemically disordered γ -phase IrMn₃ alloy, below the Néel temperature T_N , the Mn moments in the fcc crystal lattice are tilted by $>45^\circ$ from the diagonal axis towards the cubic faces, as determined by neutron diffraction experiments [68]. In such a case, the FM spins at the FM/AFM interface prefer a tilted alignment towards the OOP direction. Therefore, we

TABLE I. A summary of the characteristic magnetic vortex parameters and properties of FM, FM/AFM, and AFM/FM/AFM disk structures, obtained experimentally from the combination of in-field HR-MFM imaging and nano-MOKE magnetometry.

Magnetic vortex parameters and properties	FM	FM/AFM		AFM/FM/AFM
		Disk 1	Disk 2	
cp	+1	-1	+1	+1
r_{eff} (nm)	70	110	185	175
Δd_{core} (nm)	<6	270	210	160
$\mu_0 H_n$ (mT)	14(\pm 1)	18(\pm 1)	18(\pm 1)	14(\pm 1) (FC) 18(\pm 1) (ZFC)
$\mu_0 H_a$ (mT)	15(\pm 1)	27(\pm 1)	27(\pm 1)	27(\pm 1) (FC) 31(\pm 1) (ZFC)
N_{V-AV}	2	4	3	3
V-AV stability field range (mT)	<2(\pm 1)	8(\pm 1)	8(\pm 1)	10(\pm 1) (FC) 11(\pm 1) (ZFC)
$\mu_0 H_{\text{eb}}$ (mT)	n/a	-2.5	-2.5	-4.5
$ J_{\text{eb}} $ ($\mu\text{J}/\text{m}^2$)	n/a	77.8	77.8	140
V-AV state	transformed to an <i>edge state</i> upon repeating the in-field MFM scan at \sim 16 mT	stable beyond 24 hours at \sim 26 mT		stable beyond 24 hours at \sim 30 mT

see an increase in r_{eff} and magnetic contrast corresponding to the V-AV state in the exchange coupled FM/AFM and AFM/FM/AFM disk structures.

In Table I, we present a summary of the characteristic magnetic vortex properties of the simple FM and the exchange-coupled FM/AFM and AFM/FM/AFM disk structures. In the exchange coupled FM/AFM and AFM/FM/AFM vortex structures, r_{eff} and Δd_{core} are significantly larger as compared to the simple FM case. Due to the small $\mu_0 H_{\text{eb}}$ and somewhat random nature of the AFM (IrMn) grain properties [65], r_{eff} and Δd_{core} do not show a clear monotonic dependence on the interfacial exchange energy J_{eb} [64]. Additionally, from the line profile of the buckled spin textures shown in Figs. 3(b), 3(d), 3(f), and 3(h), we extract the number of V-AV pairs N_{V-AV} formed in the FM, FM/AFM, and AFM/FM/AFM disk structures. We found a significant increase in the V-AV annihilation field in the exchange coupled FM/AFM and AFM/FM/AFM disk structures. The increase in the stability range of the intermediate V-AV state in the exchange coupled disk structures is correlated to the increase in J_{eb} .

IV. CONCLUSION

In summary, we have systematically studied the remanent vortex structure and the V-AV mediated magnetic vortex annihilation processes in NiFe (40 nm), NiFe (40 nm)/IrMn (7.5 nm), and IrMn (7.5 nm)/NiFe (40 nm)/IrMn (7.5 nm) disk structures. In the exchange coupled FM/AFM and AFM/FM/AFM disks, the distortion of the FM vortex structure is correlated to the randomly distributed nonplanar

uncompensated spins at the surface of the polycrystalline AFM layer. Analysis of the remanent high-resolution MFM images reveals a considerable increase of the effective vortex core radius in the exchange coupled disks. The deflection of the vortex core from the center of the exchange coupled disks at remanence depends on the magnitude of the exchange bias field and the AFM grain properties. At remanence, the direction of the vortex core deflection with respect to the cooling field orientation depends on the handedness of the exchange biased vortex structure. Detailed in-field MFM and MOKE magnetometry studies of the V-AV mediated magnetic vortex annihilation processes in FM, FM/AFM, and AFM/FM/AFM disk structures reveal a significant increase in the magnetic field stability of the intermediate V-AV state in exchange coupled disks. Our experimental study of the characteristic magnetic vortex parameters and properties of the exchange coupled FM/AFM and AFM/FM/AFM disk structures provide a deeper understanding of the interfacial exchange interaction between the FM vortex structure and a polycrystalline chemically disordered AFM layer.

ACKNOWLEDGMENTS

The authors would like to thank Prof. G. Salvan for facilitating access to the nano-MOKE2 setup, Prof. C. Tegenkamp for providing access to the SEM facilities at TU Chemnitz, and technical support from Dr. M. Lenz at the HZDR facilities. Additionally, the authors would like to acknowledge discussions with Dr. J. Lindner from HZDR and Dr. S. Wintz from PSI.

- [1] W. H. Meiklejohn and C. P. Bean, New magnetic anisotropy, *Phys. Rev.* **102**, 1413 (1956).
- [2] J. Železný, P. Wadley, K. Olejník, A. Hoffmann, and H. Ohno, Spin transport and spin torque in antiferromagnetic devices, *Nat. Phys.* **14**, 220 (2018).
- [3] M. Bode, E. Y. Vedmedenko, K. von Bergmann, A. Kubetzka, P. Ferriani, S. Heinze, and R. Wiesendanger, Atomic spin struc-

ture of antiferromagnetic domain walls, *Nat. Mater.* **5**, 477 (2006).

- [4] T. Kosub, M. Kopte, R. Hühne, P. Appel, B. Shields, P. Maletinsky, R. Hübner, M. O. Liedke, J. Fassbender, O. G. Schmidt, and D. Makarov, Purely antiferromagnetic magnetoelectric random access memory, *Nat. Commun.* **8**, 13985 (2017).

- [5] S. Fukami, C. Zhang, S. Dutta Gupta, A. Kurenkov, and H. Ohno, Magnetization switching by spin-orbit torque in an antiferromagnet-ferromagnet bilayer system, *Nat. Mater.* **15**, 535 (2016).
- [6] F. Garcia-Sanchez, J. Sampaio, N. Reyren, V. Cros, and J.-V. Kim, A skyrmion-based spin-torque nano-oscillator, *New J. Phys.* **18**, 075011 (2019).
- [7] A. Chanthbouala, R. Matsumoto, J. Grollier, V. Cros, A. Anane, A. Fert, A. V. Khvalkovskiy, K. A. Zvezdin, K. Nishimura, Y. Nagamine, H. Maehara, K. Tsunekawa, A. Fukushima, and S. Yuasa, Vertical-current-induced domain-wall motion in MgO-based magnetic tunnel junctions with low current densities, *Nat. Phys.* **7**, 626 (2011).
- [8] D. Suess, A. Bachleitner-Hofmann, A. Satz, H. Weitenfelder, C. Vogler, F. Bruckner, C. Abert, K. Prügl, J. Zimmer, C. Huber, S. Lubner, W. Raberg, T. Schrefl, and H. Brück, Topologically protected vortex structures for low-noise magnetic sensors with high linear range, *Nat. Electron.* **1**, 362 (2018).
- [9] J. Grollier, D. Querlioz, K. Y. Camsari, K. Everschor-Sitte, S. Fukami, and M. D. Stiles, Neuromorphic spintronics, *Nat. Electron.* **3**, 360 (2020).
- [10] G. Yu, A. Jenkins, X. Ma, S. A. Razavi, C. He, G. Yin, Q. Shao, Q. L. He, H. Wu, W. Li, W. Jiang, X. Han, X. Li, A. C. B. Jayich, P. K. Amiri, and K. L. Wang, Room-temperature skyrmions in an antiferromagnet-based heterostructure, *Nano Lett.* **18**, 980 (2018).
- [11] F. P. Chmiel, N. Waterfield Price, R. D. Johnson, A. D. Lamir, J. Schad, G. van der Laan, D. T. Harris, J. Irwin, M. S. Rzechowski, C.-B. Eom, and P. G. Radaelli, Observation of magnetic vortex pairs at room temperature in a planar α -Fe₂O₃/Co heterostructure, *Nat. Mater.* **17**, 581 (2018).
- [12] E. Albisetti, A. Calò, M. Spieser, A. W. Knoll, E. Riedo, and D. Petti, Stabilization and control of topological magnetic solitons via magnetic nanopatterning of exchange bias systems, *Appl. Phys. Lett.* **113**, 162401 (2018).
- [13] D. Mitin, A. Kovacs, T. Schrefl, A. Ehresmann, D. Holzinger, and M. Albrecht, Magnetic properties of artificially designed magnetic stray field landscapes in laterally confined exchange-bias layers, *Nanotechnology* **29**, 355708 (2018).
- [14] E. Albisetti, D. Petti, M. Pancaldi, M. Madami, S. Tacchi, J. Curtis, W. P. King, A. Papp, G. Csaba, W. Porod, P. Vavassori, E. Riedo, and R. Bertacco, Nanopatterning reconfigurable magnetic landscapes via thermally assisted scanning probe lithography, *Nat. Nano.* **11**, 545 (2016).
- [15] E. Albisetti, D. Petti, G. Sala, R. Silvani, S. Tacchi, S. Finizio, S. Wintz, A. Calò, X. Zheng, J. Raabe, E. Riedo, and R. Bertacco, Nanoscale spin-wave circuits based on engineered reconfigurable spin-textures, *Commun. Phys.* **1**, 56 (2018).
- [16] E. Albisetti, S. Tacchi, R. Silvani, G. Scaramuzzi, S. Finizio, S. Wintz, C. Rinaldi, M. Cantoni, J. Raabe, G. Carlotti, R. Bertacco, E. Riedo, and D. Petti, Optically inspired nanomagnonics with nonreciprocal spin waves in synthetic antiferromagnets, *Adv. Mater.* **32**, 1906439 (2020).
- [17] D. A. Gilbert, L. Ye, A. Varea, S. Agramunt-Puig, N. D. Valle, C. Navau, J. F. López-Barbera, K. S. Buchanan, A. Hoffmann, A. Sánchez, J. Sort, K. Liu, and J. Nogués, A new reversal mode in exchange coupled antiferromagnetic/ferromagnetic disks: Distorted viscous vortex, Magnetization Reversal in Submicron Disks: Exchange Biased Vortices, *Nanoscale* **7**, 9878 (2015).
- [18] J. Sort, A. Hoffmann, S.-H. Chung, K. S. Buchanan, M. Grimsditch, M. D. Baró, B. Dieny, and J. Nogués, Magnetization Reversal in Submicron Disks: Exchange Biased Vortices, *Phys. Rev. Lett.* **95**, 067201 (2005).
- [19] J. Sort, G. Salazar-Alvarez, M. D. Baró, B. Dieny, A. Hoffmann, V. Novosad, and J. Nogués, Controlling magnetic vortices through exchange bias, *Appl. Phys. Lett.* **88**, 042502 (2006).
- [20] J. Sort, K. S. Buchanan, V. Novosad, A. Hoffmann, G. Salazar-Alvarez, A. Bollero, M. D. Baró, B. Dieny, and J. Nogués, Imprinting Vortices into Antiferromagnets, *Phys. Rev. Lett.* **97**, 067201 (2006).
- [21] K. Yu. Guslienko and A. Hoffmann, Field Evolution of Tilted Vortex Cores in Exchange-Biased Ferromagnetic Dots, *Phys. Rev. Lett.* **97**, 107203 (2006).
- [22] K. Y. Guslienko and A. Hoffmann, Vortex magnetization reversal in double-layer ferromagnetic/antiferromagnetic dots, *J. Appl. Phys.* **101**, 093901 (2007).
- [23] M. Tanase, A. K. Petford-Long, O. Heinonen, K. S. Buchanan, J. Sort, and J. Nogués, Magnetization reversal in circularly exchange-biased ferromagnetic disks, *Phys. Rev. B* **79**, 014436 (2009).
- [24] W. Jung, F. J. Castano, and C. A. Ross, Vortex Chirality in Exchange-Biased Elliptical Magnetic Rings, *Phys. Rev. Lett.* **97**, 247209 (2006).
- [25] J. Wu, D. Carlton, J. S. Park, Y. Meng, E. Arenholz, A. Doran, A. T. Young, A. Scholl, C. Hwang, H. W. Zhao, J. Bokor, and Z. Q. Qiu, Direct observation of imprinted antiferromagnetic vortex states in CoO/Fe/Ag(001) discs, *Nat. Phys.* **7**, 303 (2011).
- [26] G.-W. Chern, H. Youk, and O. Tchernyshyov, Topological defects in flat nanomagnets: The magnetostatic limit, *J. Appl. Phys.* **99**, 08Q505 (2006).
- [27] R. Hertel and C. M. Schneider, Exchange Explosions: Magnetization Dynamics During Vortex-Antivortex Annihilation, *Phys. Rev. Lett.* **97**, 177202 (2006).
- [28] O. A. Tretiakov and O. Tchernyshyov, Vortices in thin ferromagnetic films and the skyrmion number, *Phys. Rev. B* **75**, 012408 (2007).
- [29] T. Shinjo, T. Okuno, R. Hassdorf, K. Shigeto, and T. Ono, Magnetic vortex core observation in circular dots of permalloy, *Science* **289**, 930 (2000).
- [30] S. K. Kim and O. Tchernyshyov, Pinning of a Bloch point by an atomic lattice, *Phys. Rev. B* **88**, 174402 (2013).
- [31] A. Thiaville and J. Miltat, in *Topology in Magnetism*, edited by J. Zang, V. Cros, and A. Hoffmann (Springer International, Cham, 2018), p. 62.
- [32] Mi-Y. Im, P. Fischer, K. Yamada, T. Sato, S. Kasai, Y. Nakatani, and T. Ono, Symmetry breaking in the formation of magnetic vortex states in a permalloy nanodisk, *Nat. Commun.* **3**, 983 (2012).
- [33] S. B. Choe, Y. Acremann, A. Scholl, A. Bauer, A. Doran, J. Stöhr, and H. A. Padmore, Vortex core-driven magnetization dynamics, *Science* **304**, 420 (2004).
- [34] S. Bohlens, B. Krüger, A. Drews, M. Bolte, G. Meier, and D. Pfannkuche, Current controlled random-access memory based on magnetic vortex handedness, *Appl. Phys. Lett.* **93**, 142508 (2008).
- [35] A. B. Butenko, A. A. Leonov, A. N. Bogdanov, and U. K. Röbler, Theory of vortex states in magnetic nanodisks with

- induced dzyaloshinskii-moriya interactions, *Phys. Rev. B* **80**, 134410 (2009).
- [36] Y. M. Luo, C. Zhou, C. Won, and Y. Z. Wu, Effect of dzyaloshinskii–moriya interaction on magnetic vortex, *AIP Adv.* **4**, 047136 (2014).
- [37] B. Van Waeyenberge, A. Puzic, H. Stoll, K. W. Chou, T. Tylliszczak, R. Hertel, M. Fähnle, H. Brückl, K. Rott, G. Reiss, I. Neudecker, D. Weiss, C. H. Back, and G. Schütz, Magnetic vortex core reversal by excitation with short bursts of an alternating field, *Nature (London)* **444**, 461 (2006).
- [38] R. Hertel, S. Gliga, M. Fähnle, and C. M. Schneider, Ultrafast Nanomagnetic Toggle Switching of Vortex Cores, *Phys. Rev. Lett.* **98**, 117201 (2007).
- [39] A. Vansteenkiste, K. W. Chou, M. Weig, M. Curcic, V. Sackmann, H. Stoll, T. Tylliszczak, G. Woltersdorf, C. H. Back, G. Schütz, and B. Van Waeyenberge, X-ray imaging of the dynamic magnetic vortex core deformation, *Nat. Phys.* **5**, 332 (2009).
- [40] E. Feldtkeller, Mikromagnetisch stetige und unstetige Magnetisierungskonfigurationen, *Z. Angew. Phys.* **19**, 530 (1965) [English translation: Continuous and singular micromagnetic configurations, *IEEE Trans. Magn.* **53**, 0700308 (2017)].
- [41] W. Döring, Point singularities in micromagnetism, *J. Appl. Phys.* **39**, 1006 (1968).
- [42] A. Thiaville, J. M. García, R. Dittrich, J. Miltat, and T. Schrefl, Micromagnetic study of bloch-point-mediated vortex core reversal, *Phys. Rev. B* **67**, 094410 (2003).
- [43] C. Donnelly, M. Guizar-Sicairos, V. Scagnoli, S. Gliga, M. Holler, J. Raabe, and L. J. Heyderman, Three-dimensional magnetization structures revealed with X-ray vector nanotomography, *Nature (London)* **547**, 328 (2017).
- [44] P. Milde, D. Köhler, J. Seidel, L. M. Eng, A. Bauer, A. Chacon, J. Kindervater, S. Mühlbauer, C. Pfeleiderer, S. Buhr, C. Schütte, and A. Rosch, Unwinding of a skyrmion lattice by magnetic monopoles, *Science* **340**, 1076 (2013).
- [45] A. Wachowiak, J. Wiebe, M. Bode, O. Pietzsch, M. Morgenstern, and R. Wiesendanger, Direct observation of internal spin structure of magnetic vortex cores, *Science* **298**, 577 (2002).
- [46] K. Y. Guslienko, V. Novosad, Y. Otani, H. Shima, and K. Fukamichi, Field evolution of magnetic vortex state in ferromagnetic disks, *Appl. Phys. Lett.* **78**, 3848 (2001).
- [47] R. P. Cowburn, D. K. Koltsov, A. O. Adeyeye, M. E. Well, and D. M. Tricker, Single-Domain Circular Nanomagnets, *Phys. Rev. Lett.* **83**, 1042 (1999).
- [48] See Supplemental Material at <http://link.aps.org/supplemental/10.1103/PhysRevB.103.014405> for x-ray diffraction measurements and rocking scans for the reference sample, Ta (8 nm)/Pt (2 nm)/IrMn (7.5nm)/NiFe (40 nm)/Ta(5 nm)/SiO₂/Si-substrate. We present micromagnetic simulation results, including a detailed list of material parameters, IP and OOP magnetization components, and micromagnetic energy terms for the magnetic vortex annihilation mediated by the V-AV pairs. It also includes SEM images for the patterned disk arrays used in the experiments, various BP configurations, and Refs. [30,42,68]. Additionally, we present a Supplemental Movie for the magnetic vortex annihilation mediated by the V-AV pairs in exchange coupled FM/AFM disk structures.
- [49] S. Brems, K. Temst, and C. V. Haesendonck, Origin of the Training Effect and Asymmetry of the Magnetization in Polycrystalline Exchange Bias Systems, *Phys. Rev. Lett.* **99**, 067201 (2007).
- [50] I. L. Guhr, O. Hellwig, C. Brombacher, and M. Albrecht, Observation of perpendicular exchange bias in [Pd/Co]–CoO nanostructures: Dependence on size, cooling field, and training, *Phys. Rev. B* **76**, 064434 (2007).
- [51] H. J. Hug, B. Stiefel, P. J. A. van Schendel, A. Moser, R. Hofer, S. Martin, and H.-J. Güntherodt, Quantitative magnetic force microscopy on perpendicularly magnetized samples, *J. Appl. Phys.* **83**, 5609 (1998).
- [52] T. Alvarez, S. V. Kalinin, and D. A. Bonnell, Magnetic-field measurements of current-carrying devices by force-sensitive magnetic-force microscopy with potential correction, *Appl. Phys. Lett.* **78**, 1005 (2001).
- [53] A. Vansteenkiste, J. Leliaert, M. Dvornik, M. Helsen, F. Garcia-Sanchez, and B. Van Waeyenberge, The design and verification of MuMax3, *AIP Adv.* **4**, 107133 (2014).
- [54] A. Hubert and R. Schäfer, *Magnetic Domains: The Analysis of the Magnetic Microstructures* (Springer-Verlag, Berlin, 1998).
- [55] M. Langer, K. Wagner, T. Sebastian, R. Hübner, J. Grenzer, Y. Wang, T. Kubota, T. Schneider, S. Stienen, K. Lenz, H. Schultheiß, J. Lindner, K. Takanashi, R. E. Arias, and J. Fassbender, Parameter-free determination of the exchange constant in thin films using magnonic patterning, *Appl. Phys. Lett.* **108**, 102402 (2016).
- [56] V. L. Mironov and O. L. Yermolaeva, Interaction of a magnetic vortex with the probe field of a magnetic force microscope, *J. Synch. Investig.* **1**, 466 (2007).
- [57] M. Noske, H. Stoll, M. Fähnle, R. Hertel, and G. Schütz, Mechanisms for the symmetric and antisymmetric switching of a magnetic vortex core: Differences and common aspects, *Phys. Rev. B* **91**, 014414 (2015).
- [58] R. Salikhov, A. Alekhin, T. Parpiiev, T. Pezeril, D. Makarov, R. Abrudan, R. Meckenstock, F. Radu, M. Farle, H. Zabel, and V. V. Temnov, Gilbert damping in NiFeGd compounds: Ferromagnetic resonance versus time-resolved spectroscopy, *Phys. Rev. B* **99**, 104412 (2019).
- [59] M. Hayashi, L. Thomas, C. Rettner, R. Moriya, and S. S. P. Parkin, Direct observation of the coherent precession of magnetic domain walls propagating along permalloy nanowires, *Nat. Phys.* **3**, 21 (2007).
- [60] V. Sluka, T. Schneider, R. A. Gallardo, A. Kákay, M. Weig, T. Warnatz, R. Mattheis, A. Roldán-Molina, P. Leros, V. Tiberkevich, A. Slavin, G. Schütz, A. Erbe, A. M. Deac, J. Lindner, J. Raabe, J. Fassbender, and S. Wintz, Emission and propagation of 1D and 2D spin waves with nanoscale wavelengths in anisotropic spin textures, *Nat. Nanotechnol.* **14**, 328 (2019).
- [61] N. Sato, K. Schultheiss, L. Körber, N. Puwenberg, T. Mühl, A. A. Awad, S. S. P. K. Arekapudi, O. Hellwig, J. Fassbender, and H. Schultheiss, Domain Wall Based Spin-Hall Nano-Oscillators, *Phys. Rev. Lett.* **123**, 057204 (2019).
- [62] Mi-Y. Im, H.-S. Han, M.-S. Jung, Y.-S. Yu, S. Lee, S. Yoon, W. Chao, P. Fischer, H. Jung-II, and K. S. Lee, Dynamics of the Bloch point in an asymmetric permalloy disk, *Nat. Commun.* **10**, 593 (2019).

- [63] T. Okuno, K. Mibu, and T. Shinjo, Two types of magnetic vortex cores in elliptical permalloy dots, *J. Appl. Phys.* **95**, 3612 (2004).
- [64] F. Radu and H. Zabel, Exchange bias effect of ferro-/antiferromagnetic heterostructure, *Springer Tr. Mod. Phys.* **227**, 97 (2008).
- [65] J. N. Rigue, F. Beck, A. M. H. de rade, P. R. Kern, J. V. Siqueira, and M. Carara, Exchange bias in bilayer and multilayer NiFe/IrMn, *IEEE Magn. Lett.* **6**, 3800204 (2015).
- [66] X. Ma, G. Yu, S. A. Razavi, S. S. Sasaki, X. Li, K. Hao, S. H. Tolbert, K. L. Wang, and X. Li, Dzyaloshinskii-Moriya Interaction across an Antiferromagnet-Ferromagnet Interface, *Phys. Rev. Lett.* **119**, 027202 (2017).
- [67] T. Yamaoka, M. Mekata, and H. Takaki, Neutron diffraction study of γ -phase Mn-Ir single crystals, *J. Phys. Soc. Jpn.* **36**, 438 (1974).
- [68] A. Kohn, A. Kovács, R. Fan, G. J. McIntyre, R. C. C. Ward, and J. P. Goff, The antiferromagnetic structures of IrMn₃ and their influence on exchange-bias, *Sci. Rep.* **3**, 2412 (2013).
- [69] B. D. Schrag, A. Anguelouch, S. Ingvarsson, G. Xiao, Y. Lu, P. L. Trouilloud, A. Gupta, R. A. Wanner, W. J. Gallagher, P. M. Rice, and S. S. P. Parkin, Néel “orange-peel” coupling in magnetic tunneling junction devices, *Appl. Phys. Lett.* **77**, 2373 (2000).
- [70] J. Moritz, F. Garcia, J. C. Toussaint, B. Dieny, and J. P. Nozières, Orange peel coupling in multilayers with perpendicular magnetic anisotropy: Application to (Co/Pt)-based exchange-biased spin-valves, *Europhys. Lett.* **65**, 123 (2004).
- [71] P. Kappenberger, S. Martin, Y. Pellmont, H. J. Hug, J. B. Kortright, O. Hellwig, and E. E. Fullerton. Direct Imaging and Determination of the Uncompensated Spin Density in Exchange-Biased CoO/(CoPt) Multilayers, *Phys. Rev. Lett.* **91**, 267202 (2003).
- [72] I. Schmid, M. A. Marioni, P. Kappenberger, S. Romer, M. Parlinska-Wojtan, H. J. Hug, O. Hellwig, M. J. Carey, and E. Fullerton. Exchange Bias and Domain Evolution at 10 nm Scales, *Phys. Rev. Lett.* **105**, 197201 (2010).
- [73] M. S. Lund, W. A. A. Macedo, K. Liu, J. Nogués, I. K. Schuller, and C. Leighton, Effect of anisotropy on the critical antiferromagnet thickness in exchange-biased bilayers, *Phys. Rev. B* **66**, 054422 (2002).
- [74] S. Brück, G. Schütz, E. Goering, X. Ji, and K. Krishnan, Uncompensated Moments in the MnPd/Fe Exchange Bias System, *Phys. Rev. Lett.* **101**, 126402 (2008).
- [75] H. Ohldag, A. Scholl, F. Nolting, E. Arenholz, S. Maat, A. T. Young, M. Carey, and J. Stöhr, Correlation between Exchange Bias and Pinned Interfacial Spins, *Phys. Rev. Lett.* **91**, 017203 (2003).
- [76] M. Fitzsimmons, B. Kirby, S. Roy, Z.-P. Li, I. Roshchin, S. Sinha, and I. Schuller, Pinned magnetization in the antiferromagnet and ferromagnet of an exchange bias system, *Phys. Rev. B* **75**, 214412 (2007).
- [77] C. Holl, M. Knol, M. Pratzner, J. Chico, I. L. Fernes, S. Lounis, and M. Morgenstern, Probing the pinning strength of magnetic vortex cores with sub-nanometer resolution, *Nat. Commun.* **11**, 2833 (2020).
- [78] J. M. García-Martín, A. Thiaville, J. Miltat, T. Okuno, L. Vila, and L. Piraux, Imaging magnetic vortices by magnetic force microscopy: Experiments and modelling, *J. Phys. D: Appl. Phys.* **37**, 965 (2004).
- [79] A. Thiaville, J. Miltat, and J. M. García, in *Magnetic Force Microscopy: Images of Nanostructures Contrast Modeling*, edited by H. Hopster, and H. P. Oepen (Springer, Berlin, 2005), pp. 225–251.
- [80] N. A. Usov and S. E. Peschany, Magnetization curling in a fine cylindrical particle, *J. Magn. Magn. Mater.* **118**, L290 (1993).
- [81] P. Fischer, Mi-Y. Im, S. Kasai, K. Yamada, T. Ono, and A. Thiaville, X-ray imaging of vortex cores in confined magnetic structures, *Phys. Rev. B* **83**, 212402 (2011).